J Mater Sci (2013) 48:441–450
DOI 10.1007/s10853-012-6758-7

Preparation and characterization of $La_{1-x}Sr_xFeO_3$ materials and their formaldehyde gas-sensing properties

Peng-Jun Yao · Jing Wang · Wen-Ling Chu · Yu-Wen Hao

Received: 3 April 2012 / Accepted: 19 July 2012 / Published online: 31 July 2012

Abstract $La_{1-x}Sr_xFeO_3$ ($x = 0.0$–1.0) nanoparticles have been synthesized by a sol–gel method. The samples are characterized by thermogravimetric/differential thermal analysis (TG/DTA), X-ray diffraction (XRD), fourier transform infrared spectroscopy (FTIR), scanning electron microscopy (SEM), and transmission electron microscopy (TEM). The $La_{1-x}Sr_xFeO_3$ ($x = 0.0$–1.0) materials have been sintered at 650 °C. Both the structural properties and phase transitions with increasing strontium content in $La_{1-x}Sr_xFeO_3$ are presented by analysis of XRD data. Formaldehyde gas-sensing properties of $La_{1-x}Sr_xFeO_3$ have been investigated. The experimental results show that the optimum operating temperatures of $La_{1-x}Sr_xFeO_3$ varies with Sr content of x. Among all the samples, $La_{0.7}Sr_{0.3}FeO_3$ shows a maximum response to formaldehyde. Finally, the formaldehyde gas-sensing mechanism has been presented.

Introduction

Formaldehyde (HCHO), a colorless, strong-smelling gas, is one of the harmful indoor volatile organic compounds (VOCs). It, a possible carcinogen [1], can cause nervous system damage [2], immune system disorders [3], and respiratory disease [4]. The increasing concern over HCHO monitoring and control environmental pollution has generated great interest in developing new sensing materials and sensor technology in the last decade. The focus is not only on the development of new sensing materials to improve sensitivity, selectivity, and stability of sensors, but also on the development of new and better fabrication techniques to ensure reliability, safety, reproducibility, and low cost. Compared with the techniques to detect indoor HCHO [5–8], semiconductor gas sensor has been investigated extensively due to low cost, simple structure, as well as simple readout and sensor operation. Semiconductor materials for detecting HCHO include NiO [9], ZnO/$ZnSnO_3$ [10], CdO-In_2O_3 [11], NiO-doped SnO_2 [12], Ni-doped ZnO [13], MWCNTs (multi-wall carbon nanotubes)-doped SnO_2 [14], and La–Bi–Fe–O [15].

It is reported that synthetic methods have great influence on the structural and electrical properties of semiconductor oxides [16, 17]. Therefore, numerous methods have been investigated to prepare semiconductor oxides such as electrochemical synthesis [18], co-precipitation [19], solid-state reaction [20], combustion [21], hydrothermal process [22], citric-EDTA complexation [23], and sol–gel process [24]. Compared with other methods, the sol–gel process has many advantages including excellent chemical stoichiometry, lower operating temperature, convenience for controlling the process and nanoscale particles.

Perovskite-type oxides with the general formula ABO_3 (A: rare earth, B: transition metal) and $A_{1-x}A'_xBO_3$ or $AB_{1-x}B'_xO_3$ (A-site or B-site substituted ABO_3) have been widely studied in the fields of catalysts [25], fuel cells [26], and oxygen transport membranes [27]. The perovskite-type oxides have attracted much attention on gas-sensing

P.-J. Yao · J. Wang (✉) · Y.-W. Hao
School of Electronic Science and Technology, Dalian University of Technology, Dalian 116023, People's Republic of China
e-mail: wangjing@dlut.edu.cn

P.-J. Yao
School of Educational Technology, Shenyang Normal University, Shenyang 110034, People's Republic of China

W.-L. Chu
State Key Laboratory of Catalysis, Dalian Institute of Chemical Physics, Chinese Academy of Sciences, Dalian 116023, People's Republic of China

properties due to their stability and sensitivity [28, 29]. $LaFeO_3$ can be used as a sensing material for detecting humidity, CO, and ethanol vapor [30–32]. La-site or Fe-site-substituted $LaFeO_3$ has been used as ethanol or formaldehyde gas-sensing materials [33–36]. It is found that the gas-sensing behaviors vary with composition x in $A_{1-x}A'_xBO_3$ or $AB_{1-x}B'_xO_3$ materials [37, 38].

In this study, strontium-substituted $LaFeO_3$ with the general formula of $La_{1-x}Sr_xFeO_3$ ($x = 0.0$–1.0) was prepared by a sol–gel technique. The structural characteristics of $La_{1-x}Sr_xFeO_3$ were investigated using various techniques including TG/DTA, XRD, FTIR, and TEM. The HCHO sensing properties of all samples were carried out at gas concentration ranging from 10 to 100 ppm to select a suitable composition material with a low operating temperature and high sensitivity sensing. Thus, these oxides were examined as novel sensing materials to HCHO.

Experimental

Preparation of $La_{1-x}Sr_xFeO_3$ materials

$La_{1-x}Sr_xFeO_3$ ($x = 0.0$–1.0) materials were prepared by a sol–gel method with analytical grade $La(NO_3)_3{\cdot}6H_2O$, $Sr(NO_3)_2$, $Fe(NO_3)_3{\cdot}9H_2O$, and citric acid as starting materials. 18.077 g citric acid was dissolved in 25 ml deionized water to yield [citric acid] = 3.44 M and was heated to 80 °C with continuous stirring. Stoichiometric quantities of $La(NO_3)_3{\cdot}6H_2O$, $Sr(NO_3)_2$, and $Fe(NO_3)_3{\cdot}9H_2O$ were dissolved in 25 ml deionized water to yield [Fe] = 0.344 M. Then the nitrate salts solution was added dropwise into citric acid solution to make a homogeneous mixture. The mixed aqueous solution was heated with continuous stirring for about 6 h until a highly viscous gel formed. The gel was dried at 120 °C for 24 h to get dry foamy powders, followed by grinding to form a fine precursor. Finally, the precursor was calcined at 650 °C for 6 h.

Characterization of $La_{1-x}Sr_xFeO_3$ materials

X-ray diffraction (XRD) patterns of the powders were examined in 2θ region of 20–80° with a scanning speed of 4° min^{-1} on Rigaku, Model D/MAX 2400, Japan, with Cu Kα (1.5406Å) radiation. The thermal decomposition behavior of the precursor powders was recorded by means of thermogravimetry (TG) and differential thermal analysis (DTA) (TGA/SDTA851e, Mettler-Toledo, Switzerland). A heating rate of 10 °C min^{-1} was used for the measurements from room temperature to 800 °C. Fourier transform infrared spectroscopy (FTIR) spectra were measured as KBr disks using a Bruker EQUINOX 55 with a spectral range from 2000 cm^{-1} to 400 cm^{-1}. Chemical analysis was performed using a SRS 3400 X-ray fluorescence spectrometer. Transmission electron microscopy (TEM) was carried out to obtain direct information about the size and structure by Tecnai G220 S-Twin transmission electron microscope. The grains were dispersed in ethanol on a carbon-coated TEM copper grid.

Gas sensors fabrication and measurements

The as-prepared samples were mixed with deionized water and carefully ground into paste in an agate mortar. The paste was coated onto a hollow ceramic tube (Ø 1 mm × 4 mm) with two electrodes spaced 1 mm, and subsequently sintered at 600 °C for 2 h. A heater consisting of a 30 Ω resistor wire was inserted through the tube. The power consumption of the heater is 0.3 W at the working temperature of 200 °C. The electrodes and heater wires were soldered on a base element [14].

The gas-sensing properties of the gas sensor were processed in a sealed chamber of an automatic testing system. The volume of the chamber was 1200 cm^3. Figure 1 gives a sketch diagram of the measuring system [39]. Bottled formaldehyde gas with concentration of 100 ppm balanced by nitrogen vapor was used. The carrier gas was bottled synthetic clean air. Both the bottled formaldehyde gas and the bottled air were produced by Guangming Special Vapors Institute of Dalian, China. The formaldehyde gas and the air were mixed in certain ratios using two mass flow controllers (MFCs) of 200 sccm (standard cubic centimeter per minute) for both formaldehyde and air. The dry mixed gas was sent into a sealed testing chamber. For a target concentration, the flow ratio was calculated as follows:

$$C_{\mathrm{HCHO}} = \frac{\frac{V_1}{5} \times F_1}{\frac{V_1}{5} \times F_1 + \frac{V_2}{5} \times F_2} C_{\mathrm{BottledHCHO}} \quad (1)$$

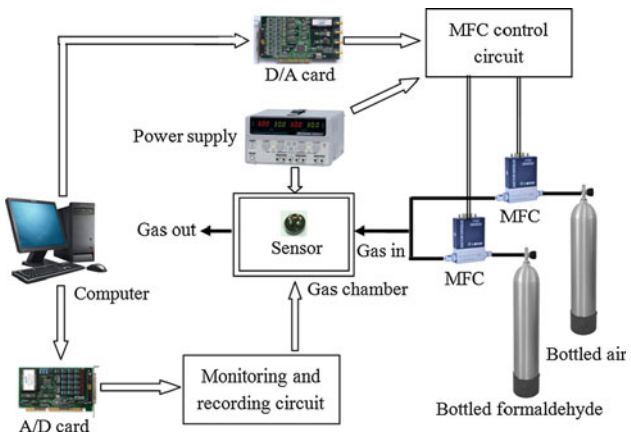

Fig. 1 Sketch diagram of the measuring system

where C_{HCHO} is the target HCHO concentration (ppm). $C_{BottledHCHO}$ is the concentration of bottled formaldehyde gas (ppm), V_1 and V_2 are two MFCs' controlling voltages (V). F_1 and F_2 are two MFCs' maximum flow (sccm). The controlling voltage was 5 V when MFC reached its highest value. $C_{BottledHCHO} = 100$ ppm and $F_1 = F_2 = 200$ sccm in this case. The procedure was as follows: pure air was introduced into the sealed chamber first. When the voltage of the sensor was stable, the detected gases were introduced into the testing chamber. Finally, the pure air was introduced for cleaning the testing chamber after the voltage of the sensor was steady in the detected gases.

The MFCs were operated by output signals of a D/A data acquisition card controlled by a computer. The change of the voltage of the sensor indicated the change of the conductivity of the sensor surface, which was caused by the change of gas concentration in the chamber. A computer monitored and recorded the change of the voltage signal by an A/D data acquisition card.

The working temperature of the sensor was provided by applying a DC power (GPS-3303C, Guwei Electronic, Taiwan) to the heater. The working temperature range of the sensor was from 160 to 440 °C. In order to improve stability and repeatability, the sensor was aged at 300 °C in air for 240 h. The sensor was connected with an external resistor in series at a voltage of 5 V. The resistance of the gas sensor in target gas is calculated as the follows: $R_S = R_L \times (5 - V_L)/V_L$, where R_S, R_L, and V_L are the resistance of the sensor, the resistance of the reference resistor, and the measured voltage, respectively. Sensor response is defined as $S = R_g/R_a$, where R_g and R_a are electrical resistance in testing gas and in air, respectively.

Results and discussion

TG/DTA analysis

Figure 2 presents thermal decomposition curves of $La_{0.8}Sr_{0.2}FeO_3$ precursor. TG curve changes slowly below 150 °C, which may be regarded as a result of evaporation of residual water in the dried precursor powders. From 150 to 460 °C, the weight loss is about 78 %, which is accompanied by two remarkable exothermic peaks around 250 °C and 360 °C depicted in DTA curve. The first exothermic reaction, between 150 and 305 °C, is mainly due to the decomposition of the organic compound. The second one, from 305 to 460 °C, is attributed to the process of formation of perovskite crystalline structure. No further weight loss or peak appears beyond 500 °C, revealing that all the organic materials have been burnt out and there is no change in the phase of $La_{0.8}Sr_{0.2}FeO_3$. The reaction

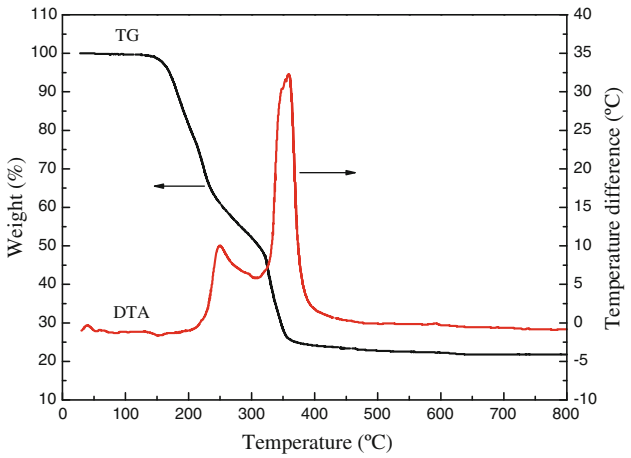

Fig. 2 TG/DTA curves of $La_{0.8}Sr_{0.2}FeO_3$ precursor

mechanism can be formulated in terms of equation as follows:

$$0.8La(NO_3)_3{\cdot}6H_2O + 0.2Sr(NO_3)_2 + Fe(NO_3)_3{\cdot}9H_2O + C_6H_8O_7 \cdot H_2O \rightarrow La_{0.8}Sr_{0.2}FeO_3 + 6CO_2 + 18.8H_2O + 2.9N_2 + 2.7O_2 \quad (2)$$

Structural properties

According to the thermal analysis of TG/DTA, 400, 500, 600, and 650 °C were selected to sinter the $La_{0.8}Sr_{0.2}FeO_3$ precursor. Figure 3 displays XRD patterns of $La_{0.8}Sr_{0.2}FeO_3$ sintered at different temperatures for 6 h. It can be seen from Fig. 3a that three broad band peaks appear at around 32°, 46°, and 57° of 2θ, respectively, which reveals that an elementary perovskite phase is formed. The major perovskite peaks (JCPDS 35-1480) are all presented in the XRD patterns of 500, 600, and 650 °C (shown in

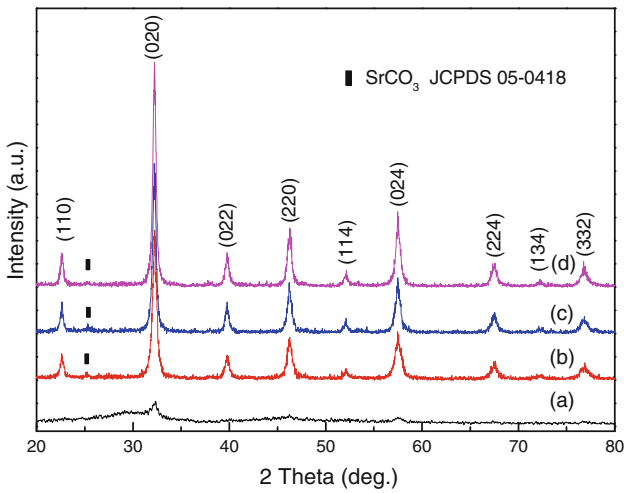

Fig. 3 XRD patterns of $La_{0.8}Sr_{0.2}FeO_3$ material sintered at different temperatures: *a* 400 °C, *b* 500 °C, *c* 600 °C, *d* 650 °C

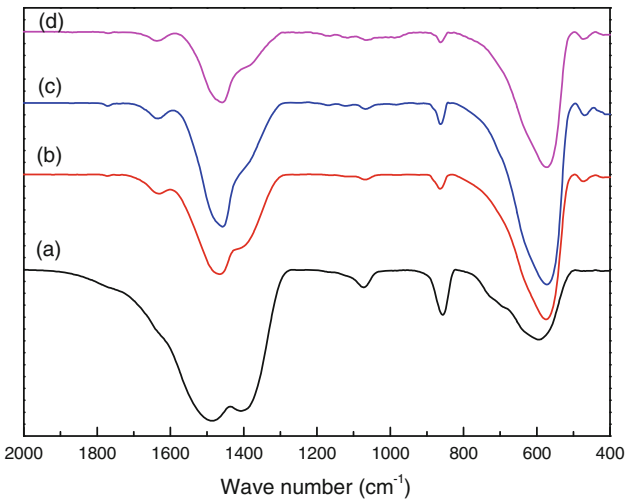

Fig. 4 FTIR spectra of $La_{0.8}Sr_{0.2}FeO_3$ material sintered at different temperatures: *a* 400 °C, *b* 500 °C, *c* 600 °C, *d* 650 °C

Fig. 3b–d), but minor phases of $SrCO_3$ (JCPDS 05-0418) are also found in the patterns.

The FTIR spectra of $La_{0.8}Sr_{0.2}FeO_3$ precursor sintered at different temperature in the frequency range of 2000–400 cm^{-1} are shown in Fig. 4. The spectra display absorption bands at 594, 575, 573, and 573 cm^{-1} for the materials sintered at 400, 500, 600, and 650 °C, respectively. These bands are related to Fe–O stretching vibration located in the octahedral site [40, 41]. It can be inferred that the elementary perovskite phase is formed after the material was annealed at 400 °C for 6 h. Small absorption bands centered at 474, 467, and 474 cm^{-1} are shown in Fig. 4b–d, respectively. These small bands belong to the stretching vibrations of Sr^{2+} situated at 12 coordinated position [42]. With the increase of sintering temperature, the compound formation is enhanced, which can be confirmed by the adsorption bands shifting from higher frequency to lower frequency. The FTIR peaks at around 1640 cm^{-1} are attributed to the stretching vibration of O–H of adsorbed water molecules from the ambient [41]. The FTIR peaks related to SrO appear at 1072, 1068, and 1066 cm^{-1} in Fig. 4a–c, respectively, but it becomes almost flat in Fig. 4d. As shown in Fig. 4a-d, the absorption bands appearing at 1460 cm^{-1} and 860 cm^{-1} are attributed to the asymmetry vibration and out-of-plane bending vibration of CO_3^{-2} [43]. The content of $SrCO_3$ decreases as the sintering temperature increases. The results are confirmed by the appearance of $SrCO_3$ displayed in Fig. 3. These may be due to the decomposition of the organic compound during sintering process, a large number of CO_2 is released immediately, which leads to the formation of $SrCO_3$ with SrO decomposed from $Sr(NO_3)_2$. This phenomenon was also observed by J. Karpinski et al. [44, 45]. Most of the alkaline earth metal oxides and rare earth metal oxides, in particular BaO, SrO, and Re_2O_3, contain metal carbonate [46, 47].

The semi-quantitative elemental composition of the as-prepared $La_{0.8}Sr_{0.2}FeO_3$ was experimentally determined using X-ray fluorescence spectrometer. The obtained experimental stoichiometric ratio of La:Sr:Fe:O is 0.795:0.218:1:2.904, which matches the expected composition based on synthesis quantities. The partial substitutions at La-site with Sr create structural defects such as oxygen vacancies, which may greatly affect gas-sensing properties. Oxygen vacancies can act as preferential adsorption sites for gas molecules. The surface defects often dominate the electronic/chemical properties and adsorption behaviors of semiconductor oxide surfaces. Oxygen vacancies bind more tightly with gas molecules attracting more charges from the surfaces compared with oxygen-vacancy-free surface [48].

Figure 5 shows the XRD patterns of $La_{1-x}Sr_xFeO_3$ ($x = 0.0$–1.0) samples sintered at 650 °C for 6 h. The main peaks of $La_{1-x}Sr_xFeO_3$ ($x = 0.0$) are identified as $LaFeO_3$ (JCPDS 75-0541) perovskite, and the main phase in $La_{1-x}Sr_xFeO_3$ ($x = 1.0$) is confirmed as $SrFeO_{2.97}$ (JCPDS card 40-0905). All the XRD patterns of $La_{1-x}Sr_xFeO_3$ ($x = 0.1$–0.9) are similar to those of $LaFeO_3$ or $SrFeO_{2.97}$, but some impurity phases related to $SrCO_3$ (JCPDS card 05-0418) are seen in $La_{1-x}Sr_xFeO_3$ ($x = 0.3$, 0.4, 0.6–1.0),

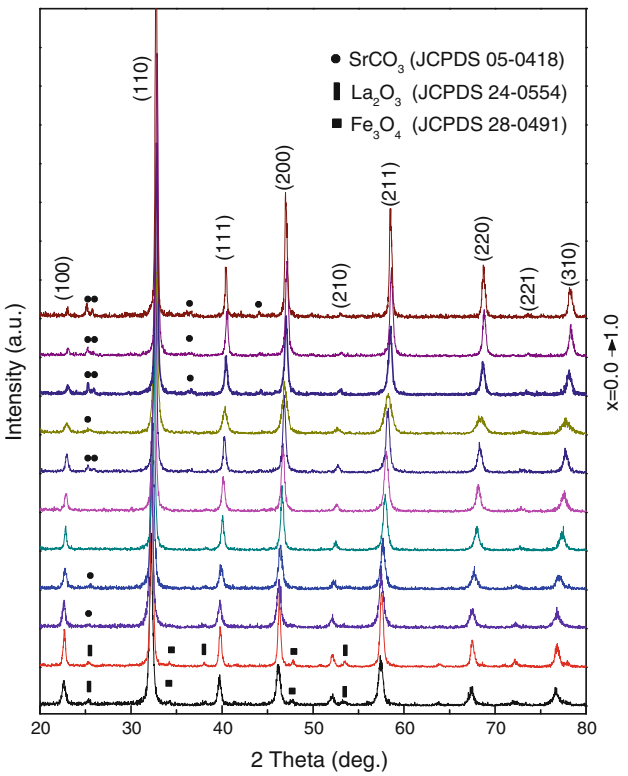

Fig. 5 XRD patterns of $La_{1-x}Sr_xFeO_3$ ($x = 0.0$–1.0) sintered at 650 °C

Table 1 XRD parameters of $La_{1-x}Sr_xFeO_3$

x	Lattice constant			Cell volume (10^{-3}nm^3)	FWHM (°)	Crystallite size (nm)	Space group	Symmetry
	a (nm)	b (nm)	c (nm)					
0.0	0.392	0.392	0.392	60.09	0.430	21.3	Pm-3m (221)	Cubic
0.1	0.554	0.553	0.789	241.71	0.437	18.9	Pnma (62)	O
0.2	0.553	0.551	0.783	238.64	0.423	19.5	Pnma (62)	O
0.3	0.552	0.549	0.782	236.84	0.421	19.6	Pnma (62)	O
0.4	0.551		1.346	354.01	0.416	19.9	R-3c (167)	R
0.5	0.550		1.343	351.56	0.367	22.5	R-3c (167)	R
0.6	0.549		1.342	350.22	0.360	26.8	R-3c (167)	R
0.7	0.548		1.340	348.44	0.510	17.5	R-3c (167)	R
0.8	0.546		0.846	218.32	0.334	29.7	R-3c (167)	R
0.9	0.545		0.836	215.32	0.322	31.4	R-3c (167)	R
1.0	0.385	0.385	0.385	57.23	0.459	18.0	Pm-3m (221)	Cubic

O Orthorhombic, *R* Rhombohedral

and some impurity peaks related to Fe_3O_4 (JCPDS 28-0491) and La_2O_3 (JCPDS 24-0554) are shown in $La_{1-x}Sr_xFeO_3$ ($x = 0.0$ and 0.1). However, no impurity phase is found in $La_{1-x}Sr_xFeO_3$ ($x = 0.4$ and 0.5). Table 1 presents the XRD parameters, such as lattice constant, cell volume, the full width at half maximum (FWHM), crystallite size, space group, and symmetry, calculated from the XRD patterns. The lattice parameters are calculated by the $d = (h^2/a^2 + k^2/b^2 + l^2/c^2)^{-1/2}$) formula from the XRD patterns. In addition, the crystallite size is evaluated by Debye Scherror formula of $0.9\lambda/\beta\cos\theta$, where λ is the wavelength of the target CuKα 1.5406 Å and β is the full width at half maximum of 32° in 2θ. The crystallite size increases with the increasing of the content of strontium except in the cases of $x = 0.7$ and the end members. Similarly, as the content of strontium increases, diffraction peaks of $La_{1-x}Sr_xFeO_3$ perovskite phase shift to higher 2θ direction, and they become correspondingly narrow. The unit cell volume decreases with the increasing of Sr content in $La_{1-x}Sr_xFeO_3$ ($x = 0.1$–0.9), indicating that the replacement of La^{3+} by Sr^{2+} leads to lattice contraction. Although the ionic radius of Sr^{2+} is larger than that of La^{3+}, the replacement of La^{3+} by Sr^{2+} in $La_{1-x}Sr_xFeO_3$ may lead to an increased covalency between the iron and oxygen ions and a decreased bond length of Fe–O due to the formation of Fe^{4+} ions, which reduces the unit cell volume [49]. Phase transitions with increasing strontium content in $La_{1-x}Sr_xFeO_3$ are displayed (see Table 1). The phase is cubic (space group Pm-3 m) for $LaFeO_3$. For $x = 0.1$–0.3, the XRD patterns are refined using an orthorhombic phase in the space group Pnma. A rhombohedral phase (space group R-3c) is observed for $x = 0.4$–0.9. A phase transition to cubic (Pm-3 m) occurs when $x = 1.0$.

The SEM micrographs of $La_{0.7}Sr_{0.3}FeO_3$ and $La_{0.8}Sr_{0.2}FeO_3$ powder sintered at 650 °C are shown in Fig. 6. These micrographs indicate agglomerated and well-defined particles with homogeneous crystallite size distribution. The porous feature of the samples may be attributed to the liberation of a large amount of gas during sintering process.

Figure 7 shows the TEM image of $La_{0.7}Sr_{0.3}FeO_3$ sample with average particle size of 20–25 nm, which is consistent with the crystallite size calculated by Debye Scherror formula of $0.9\lambda/\beta\cos\theta$ in Table 1.

Formaldehyde gas-sensing properties

Gas-sensing experiments were performed at different operating temperatures to find the optimum operating condition. Figure 8 displays the relationship between the different operating temperature and the response of $La_{1-x}Sr_xFeO_3$ ($x = 0.0$–1.0) sensors to 50 ppm HCHO. The optimum operating temperatures and the response of $La_{1-x}Sr_xFeO_3$ gas sensors are listed in Table 2. It can be seen that the optimum temperatures vary with x. Among the sensors, $La_{0.7}Sr_{0.3}FeO_3$ sensor shows the maximum response of about 26 to 50 ppm HCHO at the optimum operating temperature of 200 °C.

The responses of $La_{1-x}Sr_xFeO_3$ sensors to different HCHO concentrations at their own optimum temperatures are shown in Fig. 9. According to the relationship between the responses of the sensors and strontium content x, it can be easily seen that the sensors response curves are separated into four sets A, B, C, and D. For the sensors in sets A-C, the response of the sensors in set A is higher than those of the sensors in sets B and C, and the response of the sensors in set C is the lowest. The responses of the sensors in set A decrease with x increasing from 0.3 to 0.6 when the

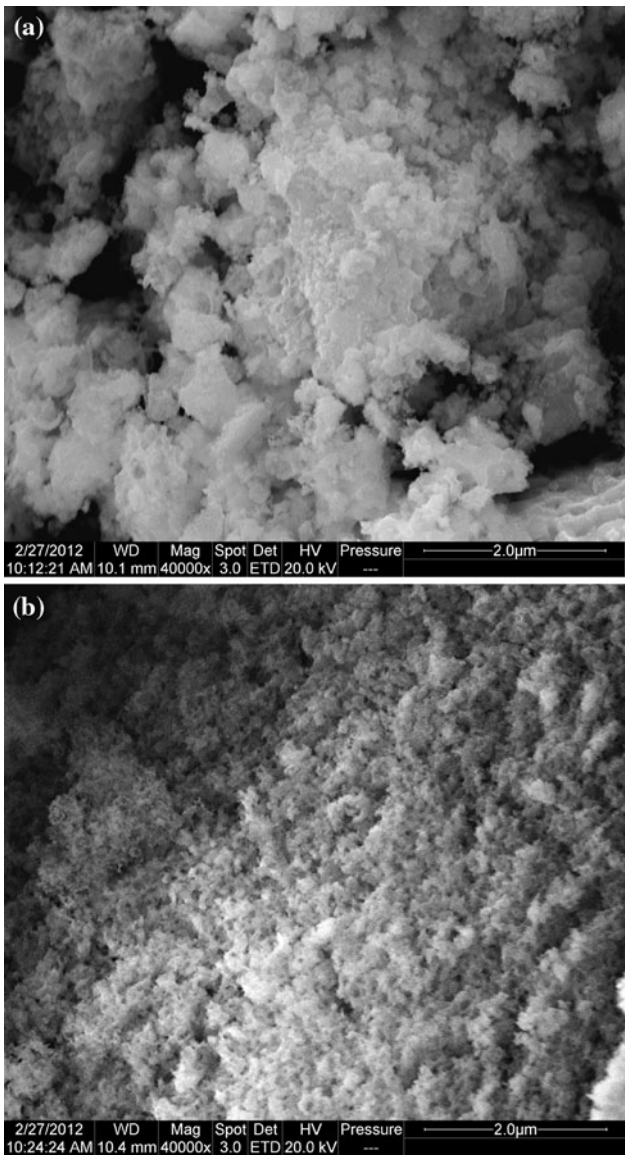

Fig. 6 SEM images of **a** $La_{0.7}Sr_{0.3}FeO_3$ and **b** $La_{0.8}Sr_{0.2}FeO_3$ powder sintered at 650 °C

sensors are exposed to 10–50 ppm HCHO. For the sensors set B, the responses decrease with x varying from 0.0 to 0.2. For the sensors in set C, the response of $La_{0.2}Sr_{0.8}FeO_3$ sensor is larger than that of $La_{0.3}Sr_{0.7}FeO_3$ sensor. All the sensors in sets A-C show a good linear relationship between the responses and HCHO concentrations. However, the sensors in set D increase rapidly from 30 to 40 ppm HCHO. The responses of the sensors in sets A-C decrease with x varying with 0.3, 0.4, 0.5, 0.6, 0.0, 0.1, 0.2, 0.8, and 0.7. Figure 9b shows the responses of $La_{0.7}Sr_{0.3}FeO_3$ sensors to 10–100 ppm HCHO concentrations at 200 °C. It is obviously found that the $La_{0.7}Sr_{0.3}FeO_3$ sensor shows the highest response to HCHO among all the $La_{1-x}Sr_xFeO_3$ ($x = 0.0$–1.0) sensors. The high difference of

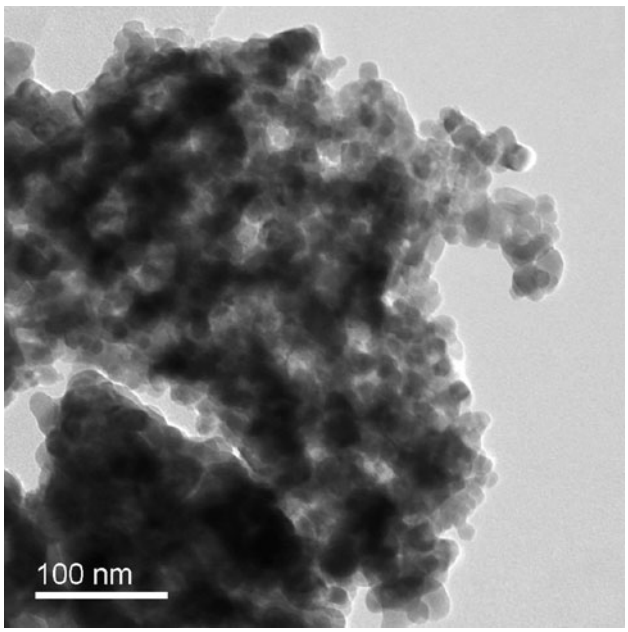

Fig. 7 TEM image of $La_{0.7}Sr_{0.3}FeO_3$ sample

$La_{1-x}Sr_xFeO_3$ sensors responses may be mainly due to the different compositions of the materials. The gas-sensing properties are relative to crystallite size, surface state, oxygen adsorption quantity, activation energy of oxygen adsorption, and lattice defects. These parameters depend on the changing composition of materials [50]. For example, with an increase in amount of Sr dopant, the optimal operating temperature of $La_xSr_{1-x}Fe_xO_3$ sensors varies, which implies that Sr doping may have an effect on the adsorption activation energy of the material.

Figure 10 illustrates the response and recovery time of $La_{0.7}Sr_{0.3}FeO_3$ gas sensor in air and in 50 ppm HCHO. The response and recovery times (defined as the time required to attain 90 % of the final value) of the sensor to 50 ppm formaldehyde are about 260 s and 70 s, respectively. The response and recover times are much longer than those of previously published (between 10 s and 60 s for different concentrations of formaldehyde [10, 12, 13, 15, 35, and 36]). This delay is due to a slow gas exchange in the test chamber concerning the volume of the chamber and the gas flow rate.

In order to study the selectivity of the $La_{0.7}Sr_{0.3}FeO_3$ gas sensor to formaldehyde, the responses of the sensor to 50 ppm acetone, ammonia, methanol, benzene, ethanol, and toluene at 200 °C were carried out. As is shown in Fig. 11, the response of the sensor to formaldehyde is higher than the responses of the sensor to other gases. The response of the sensor to formaldehyde is 26, while to acetone, ammonia, methanol, benzene, ethanol, and toluene, the responses are 9, 1.2, 10.5, 1.4, 19, and 1.5, respectively, which indicates that ethanol is the main

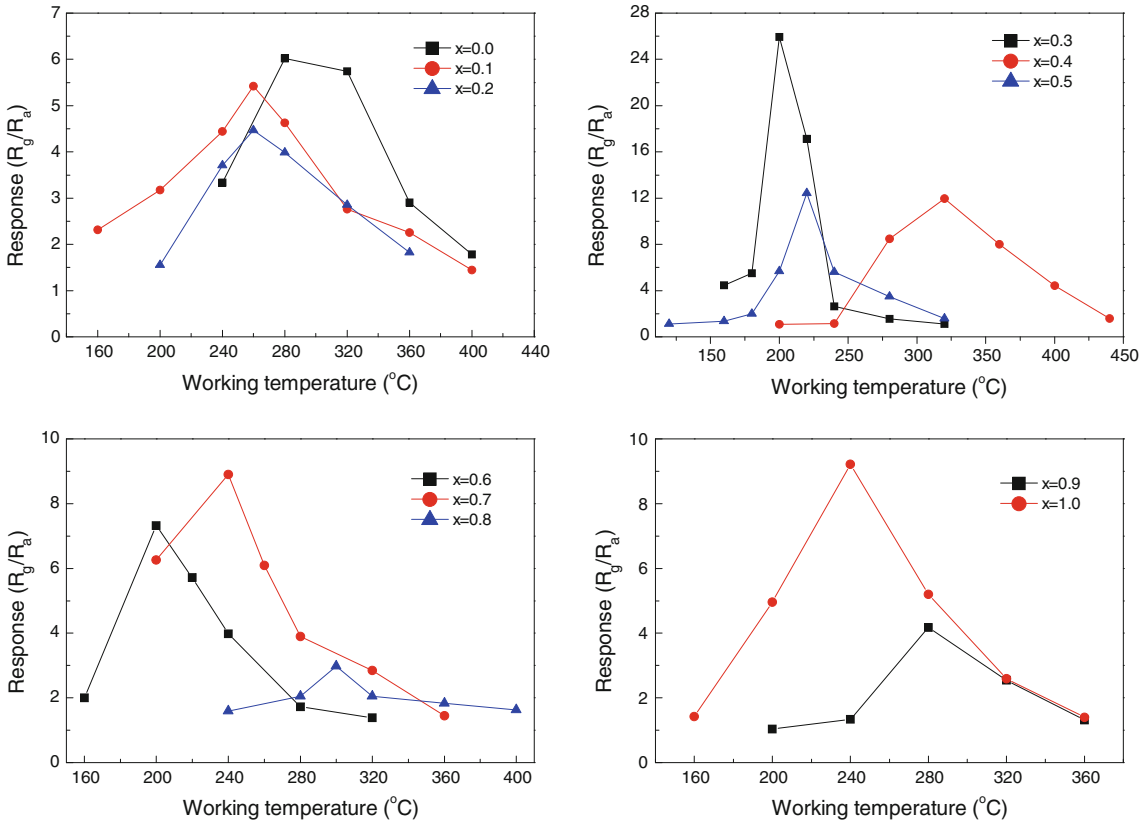

Fig. 8 The response of $La_{1-x}Sr_xFeO_3$ ($x = 0.0$–1.0) sensors to 50 ppm HCHO at different temperatures

Table 2 The optimum operating temperatures and the response of $La_{1-x}Sr_xFeO_3$ sensors

x	Temperature (°C)	Response (R_g/R_a)
0.0	280	6.0
0.1	260	5.4
0.2	260	4.5
0.3	200	26.0
0.4	320	11.9
0.5	220	12.4
0.6	200	7.3
0.7	260	6.1
0.8	300	3.0
0.9	280	4.2
1.0	240	9.2

interference gases for the sensor. Cross sensitivity is a well-known disadvantage for the metal oxide gas sensors. The selectivity of $La_{0.7}Sr_{0.3}FeO_3$ gas sensor can be improved by optimizing the doping (elements and their concentration) [51], the operation temperature [52], or neural network methods [53]. The detailed information will be discussed in future.

In order to investigate the long time stability of the $La_{0.7}Sr_{0.3}FeO_3$ gas sensors, the responses of the two sensors to 50 ppm formaldehyde were repeated every 5 days for total 30 days. Figure 12 gives the responses of two $La_{0.7}Sr_{0.3}FeO_3$ gas sensors to 50 ppm formaldehyde at 200 °C. It can be seen from the figure that each sensor exhibits a nearly constant sensor signal during the test, indicating a good stability of the $La_{0.7}Sr_{0.3}FeO_3$ gas sensors. The inset in Fig. 12 shows the transient response of the sensors to 50 ppm formaldehyde at 200 °C. The reversibility and repeatability of two $La_{0.7}Sr_{0.3}FeO_3$ gas sensors are also satisfactory.

Gas-sensing mechanism

The resistance increases when the sensors are exposed in formaldehyde, which reveals that $La_{1-x}Sr_xFeO$ ($x = 0.0$–1.0) shows p-type semiconductor conductivity behavior in formaldehyde gas. The possible formaldehyde gas-sensing mechanism is suggested as follows:

The $La_{1-x}Sr_xFeO_3$-based sensor is influenced by the oxygen adsorbed on the surface of the material. The metal

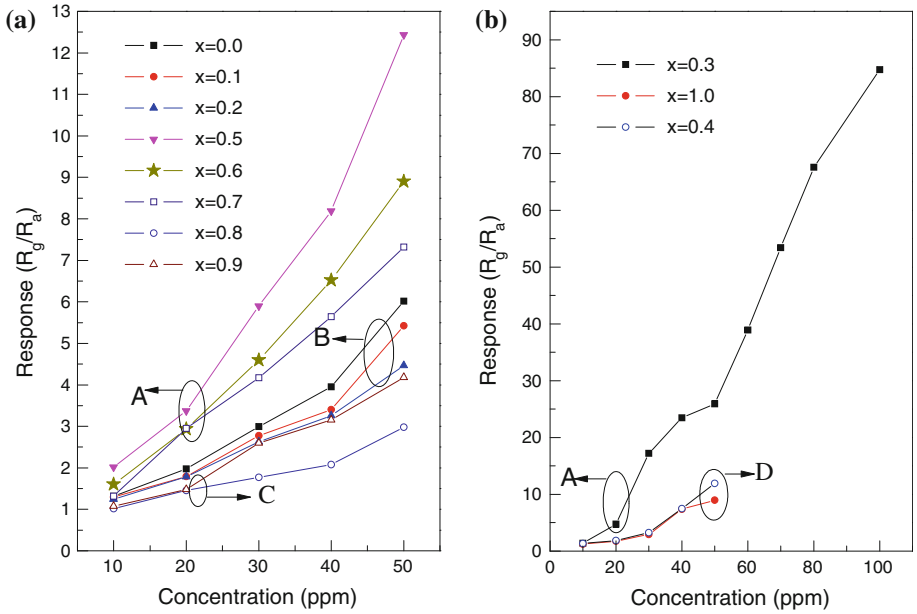

Fig. 9 The sensors responses to different HCHO concentrations at their optimum operating temperatures. **a** $La_{1-x}Sr_xFeO_3$ ($x = 0.0$–0.3, 0.5–0.9); **b** $La_{1-x}Sr_xFeO_3$ ($x = 0.3$, 0.4, 1.0)

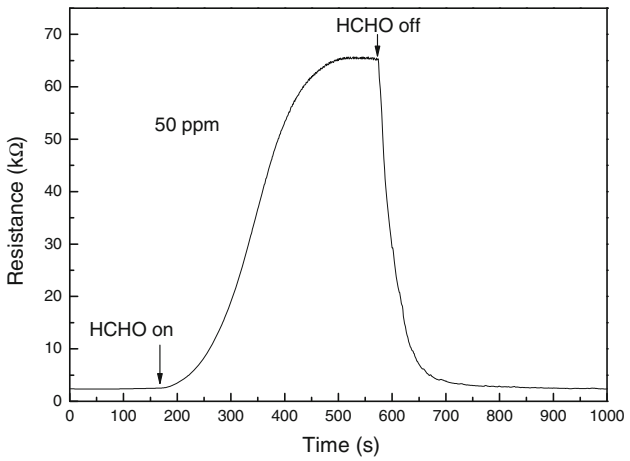

Fig. 10 Response transient of $La_{0.7}Sr_{0.3}FeO_3$ gas sensor to 50 ppm formaldehyde

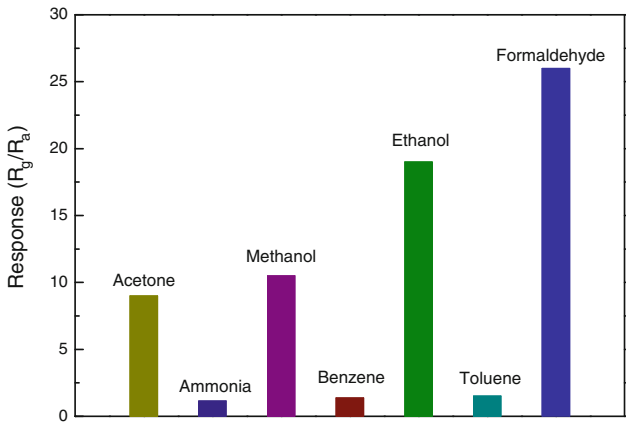

Fig. 11 Response of the $La_{0.7}Sr_{0.3}FeO_3$ gas sensor to 50 ppm acetone, ammonia, methanol, benzene, ethanol, toluene, and formaldehyde at 200 °C

ions on the surface of $La_{1-x}Sr_xFeO_3$ can adsorb atmospheric oxygen easily. The electronic states of the adsorbed oxygen species on the surface of $La_{1-x}Sr_xFeO_3$ materials undergo following reactions [54]:

$$O_{2(gas)} \leftrightarrow O_{2(ads)} \quad (3)$$

$$O_{2(ads)} + e^- \leftrightarrow O^-_{2(ads)} \quad (4)$$

$$O^-_{2(ads)} + e^- \leftrightarrow 2O^-_{(ads)} \quad (5)$$

$$O^-_{(ads)} + e^- \leftrightarrow O^{2-}_{(ads)} \quad (6)$$

where the subscripts gas and ads represent molecular oxygen and the state of adsorption, respectively. When temperature increases, the equilibrium shifts to the right. This will decrease the barrier height for a hole to transport and the oxygen species capture electrons from the sensing materials, which will lead to the decreasing of the resistance. Since adsorption is an exothermic reaction, the quantity of adsorbate decreases at higher temperature. However, since the oxidation of formaldehyde is thermally activated, the reaction rate increases depending on temperature. The response results from the interaction of the above two reactions, thus it reached to an optimum [55].

When in the presence of reducing gas HCHO, the oxygen adsorbed on the surface of the sensing material react with HCHO as follows [39, 56]:

$$(HCHO)_{ads} + O^-_{(ads)} \rightarrow CHOOH + e^- \quad (7)$$

$$(HCHO)_{ads} + 2O^{2-}_{(ads)} \rightarrow CO_2 + H_2O + 4e^- \quad (8)$$

The products could be formic acid (CHOOH) and/or water, and CO_2. Both of these reactions release electrons.

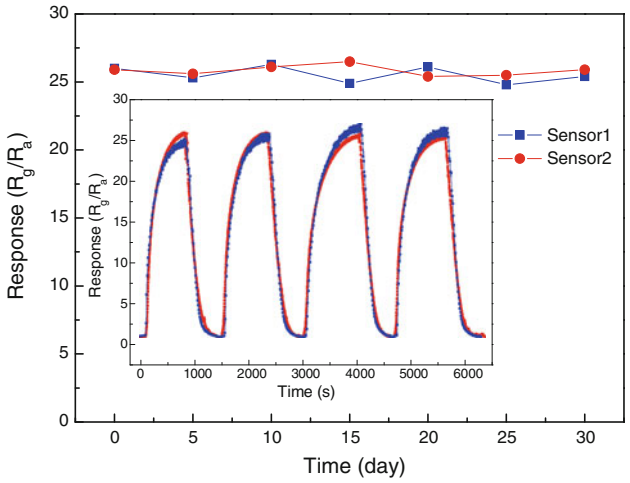

Fig. 12 Stability of $La_{0.7}Sr_{0.3}FeO_3$ gas sensors to formaldehyde for 30 days; the *inset* is the transient response of the sensors to 50 ppm formaldehyde at 200 °C

The released electrons are compensated with the holes of $La_{1-x}Sr_xFeO_3$, which leads to the decreasing of conductivity of the material. As a result, the resistance of the sensor will increase.

Conclusions

Nanocrystalline $La_{1-x}Sr_xFeO_3$ ($x = 0.0$–1.0) powders have been synthesized by a sol–gel method. It is found that the main phases of all the samples sintered at 650 °C are perovskite structures. Some impurity phases related to $SrCO_3$, Fe_3O_4, and La_2O_3 are shown in $La_{1-x}Sr_xFeO_3$ ($x = 0.0$–0.3, 0.6–1.0). However, no impurity phase is found in $La_{1-x}Sr_xFeO_3$ ($x = 0.4$, 0.5). As Sr content of x increases, the phase varies with cubic, orthorhombic, and rhombohedral and cubic phase. XRD data and TEM images confirm that the average crystallite size of $La_{0.7}Sr_{0.3}FeO_3$ is about 25 nm. The $La_{1-x}Sr_xFeO_3$ materials present a *p*-type semiconductor behavior in formaldehyde. The optimum working temperatures of $La_{1-x}Sr_xFeO_3$ change with composition x, and the responses of $La_{1-x}Sr_xFeO_3$ to HCHO depend on composition x. Among $La_{1-x}Sr_xFeO_3$ ($x = 0.0$–1.0) materials, $La_{0.7}Sr_{0.3}FeO_3$ shows the maximum response of about 26 to 50 ppm HCHO at the optimum operating temperature of 200 °C. The response and recovery times of $La_{0.7}Sr_{0.3}FeO_3$ to 50 ppm HCHO are 260 s and 70 s, respectively. Ethanol is the main interference gases for the $La_{0.7}Sr_{0.3}FeO_3$ sensor.

Acknowledgements This subject was supported by the National Natural Science Foundation of China (61176068, 61131004). The authors thank Mr. Xing-Ru Chen for his help in the experiments. The authors are grateful to the anonymous reviewers for their valuable corrections and suggestions.

References

1. Soffritti M, Maltoni C, Maffei F, Biagi R (1989) Toxicol Ind Health 5:699. doi:10.1177/074823378900500510
2. Songur A, Ozen OA, Sarsilmaz M (2010) Rev Environ Contam Toxicol 203:105. doi:10.1007/978-1-4419-1352-4_3
3. Thrasher JD, Broughton A, Madison R (1990) Arch Environ Health 45:217. doi:10.1080/00039896.1990.9940805
4. Subramaniam RP, Chen C, Crump KS, DeVoney D, Fox JF, Portier CJ, Schlosser PM, Thompson CM, White P (2008) Risk Anal 28:907. doi:10.1111/j.1539-6924.2008.01083.x
5. Kuijpers ATJM, Neele J (1983) Anal Chem 55:390. doi:10.1021/ac00253a052
6. Hunter MC, Bartle KD, Seakins PW, Lewis AC (1999) Anal Commun 36:101. doi:10.1039/A809762C
7. Septon JC, Ku JC (1982) Am Ind Hyg Assoc J 43:845. doi:10.1080/15298668291410675
8. Kim S, Kim HJ (2005) Bioresour Technol 96:1457. doi:10.1016/j.biortech.2004.12.003
9. Dirksen JA, Duval K, Ring TA (2001) Sens Actuators B 80:106. doi:10.1016/S0925-4005(01)00898-X
10. Xu JQ, Jia XH, Lou XD, Xi GX, Han JJ, Gao QH (2007) Sens Actuators B 120:694. doi:10.1016/j.snb.2006.03.033
11. Chen T, Liu QJ, Zhou ZL, Wang YD (2008) Sens Actuators B 131:301. doi:10.1016/j.snb.2007.11.025
12. Lv P, Tang ZA, Yu J, Zhang FT, Wei GF, Huang ZX, Hu Y (2008) Sens Actuators B 132:74. doi:10.1016/j.snb.2008.01.018
13. Bai ZK, Xie CS, Hu ML, Zhang SP (2008) Physica E 41:235. doi:10.1016/j.physe.2008.07.019
14. Wang J, Liu L, Cong SY, Qi JQ, Xu BK (2008) Sens Actuators B 134:1010. doi:10.1016/j.snb.2008.07.010
15. Ruan QJ, Zhang WD (2008) Mater Lett 62:4303. doi:10.1016/j.matlet.2008.07.012
16. Polini R, Pamio A, Traversa E (2004) J Eur Ceram Soc 24:1365. doi:10.1016/S0955-2219(03)00592-2
17. Hien NT, Thuy NP (2002) Phys B 319:168. doi:10.1016/S0921-4526(02)01118-3
18. Therese GHA, Dinamani M, Kamath PV (2005) J Appl Electrochem 35:459. doi:10.1007/s10800-004-8346-2
19. Vladimirova E, Vassiliev V, Nossov A (2001) J Mater Sci 36:1481. doi:10.1023/A:1017548813705
20. Lee S, Lee KS, Woo SK, Kim JW, Ishihara T, Kim DK (2003) Solid State Ionics 158:287. doi:10.1016/S0167-2738(02)00821-4
21. Manoharan SS, Patil KC (1993) J Solid State Chem 102:267. doi:10.1006/jssc.1993.1031
22. Woo K, Choi GJ, Sim SJ, Cho YS, Kim YD (2000) J Mater Sci 35:4539. doi:10.1023/A:1004868621334
23. Lu H, Tong J, Cong Y, Yang W (2005) Catal Today 104:154. doi:10.1016/j.cattod.2005.03.078
24. Liu J, Co AC, Paulson S, Birss VI (2006) Solid State Ionics 177:377. doi:10.1016/j.ssi.2005.11.005
25. Leontiou AA, Ladavos AK, Giannakas AE, Bakas TV, Pomonis PJ (2007) J Catal 251:103. doi:10.1016/j.jcat.2007.07.012
26. Kishimoto H, Sakai N, Horita T, Yamaji K, Brito ME, Yokokawa H (2008) Solid State Ionics 179:1338. doi:10.1016/j.ssi.2007.12.009
27. Pena MA, Fierro JLG (2001) Chem Rev 101:1981. doi:10.1021/cr980129f
28. Itagaki Y, Mori M, Hosoya Y, Aono H, Sadaoka Y (2007) Sens Actuators B 122:315. doi:10.1016/j.snb.2006.06.001
29. Zhao M, Peng H, Hu JF, Han ZX (2008) Sens Actuators B 129:953. doi:10.1016/j.snb.2007.10.012
30. Wang J, Wu FQ, Shi KH, Wang XH, Sun PP (2004) Sens Actuators B 99:586. doi:10.1016/j.snb.2004.01.012
31. Songn P, Wang Q, Zhang Z, Yang ZX (2010) Sens Actuators B 147:248. doi:10.1016/j.snb.2010.03.006

32. Fan HT, Xu XJ, Ma XK, Zhang T (2011) Nanotechnology 22:115502. doi:10.1088/0957-4484/22/11/115502
33. Liu L, Zhang T, Qi Q, Zhang L, Chen WY, Xu BK (2007) Solid-State Electron 51:1029. doi:10.1016/j.sse.2007.05.016
34. Song P, Hu JF, Qin HW, Zhang L, An K (2004) Mater Lett 58:2610. doi:10.1016/j.matlet.2004.03.028
35. Zhang L, Hu J, Song P, Qin H, Liu X, Jiang M (2005) Phys B 370:259. doi:10.1016/j.physb.2005.09.020
36. Huang SX, Qin HW, Song P, Liu X, Li L, Zhang R, Hu J, Yan H, Jiang M (2007) J Mater Sci 42:9973. doi:10.1007/s10853-007-1991-1
37. Liu X, Cheng B, Qin HW, Song P, Huang SX, Zhang R, Hu JF, Jiang MH (2008) Sens Actuators B 129:53. doi:10.1016/j.snb.2007.07.102
38. Pokhrel S, Huo LH, Zhao H, Gao S (2007) Sens Actuators B 122:321. doi:10.1016/j.snb.2006.06.003
39. Wang J, Zhang P, Qi JQ, Yao PJ (2009) Sens Actuators B 136:399. doi:10.1016/j.snb.2008.12.056
40. Augustin CO, Selvan RK, Nagaraj R, Berchmans LJ (2005) Mater Chem Phys 89:406. doi:10.1016/j.matchemphys.2004.09.028
41. Li KY, Wu FQ, Wang DJ, Xie TF, Li TJ (2001) Mater Chem Phys 71:34. doi:10.1016/S0254-0584(00)00524-1
42. Li SD, Jing LQ, Fu W, Yang LB, Xin BF, Fu HG (2007) Mater Res Bull 42:203. doi:10.1016/j.materresbull.2006.06.010
43. Tas AC, Majewski PJ, Aldinger F (2000) J Am Ceram Soc 83:2954. doi:10.1111/j.1151-2916.2000.tb01666.x
44. Karpinski J, Schwer H, Meijer GI, Conder K, Kopnin EM, Rossel C (1997) Physica C 274:99. doi:10.1016/S0921-4534(96)00670-3
45. Cizauskaite S, Kareiva A (2008) Cent Eur J Chem 6:456. doi:10.2478/s11532-008-0045-0
46. Gomes J, Pires AM, Serra OA (2006) J Fluoresc 16:411. doi:10.1007/s10895-006-0090-z
47. Kale GM, Jacob KT (1989) Solid State Ionics 34:247. doi:10.1016/0167-2738(89)90450-5
48. Ahn MW, Park KS, Heo JH, Park JG, Kim DW, Choi KJ, Lee JH, Hong SH (2008) Appl Phys Lett 93:263103. doi:10.1063/1.3046726
49. Li JG, Kou XL, Qin Y, He HY (2002) Phys Stat Sol (a) 191:255. doi:10.1002/1521-396X(200205)191:1<255:AID-PSSA255>3.0.CO;2-N
50. Xu JQ, Pan QY, Shun YA, Tian ZZ (2000) Sens Actuators B 66:277. doi:10.1016/S0925-4005(00)00381-6
51. Guo PF, Pan HB (2006) Sens Actuators B 114:762. doi:10.1016/j.snb.2005.07.040
52. Yamazoe N (1991) Sens Actuators B 5:7. doi:10.1016/0925-4005(91)80213-4
53. Zhao L, Qi JQ, Wang J, Yao PJ (2012) Meas Sci Technol 23:085101. doi:10.1088/0957-0233/23/8/085101
54. Liu X, Cheng B, Hu JF, Qin HW, Jiang MH (2008) Sens Actuators B 133:340. doi:10.1016/j.snb.2008.02.033
55. Chen YC, Chang YH, Chen GJ, Chai YL, Ray DT (2003) Sens Actuators B 96:82. doi:10.1016/S0925-4005(03)00489-1
56. Chen T, Zhou ZL, Wang YD (2009) Sens Actuators B 143:124. doi:10.1016/j.snb.2009.09.031